

Microstructure and Magnetic Properties of 6.5 Wt Pct Si Steel Strip Produced by Simulated Strip Casting Process



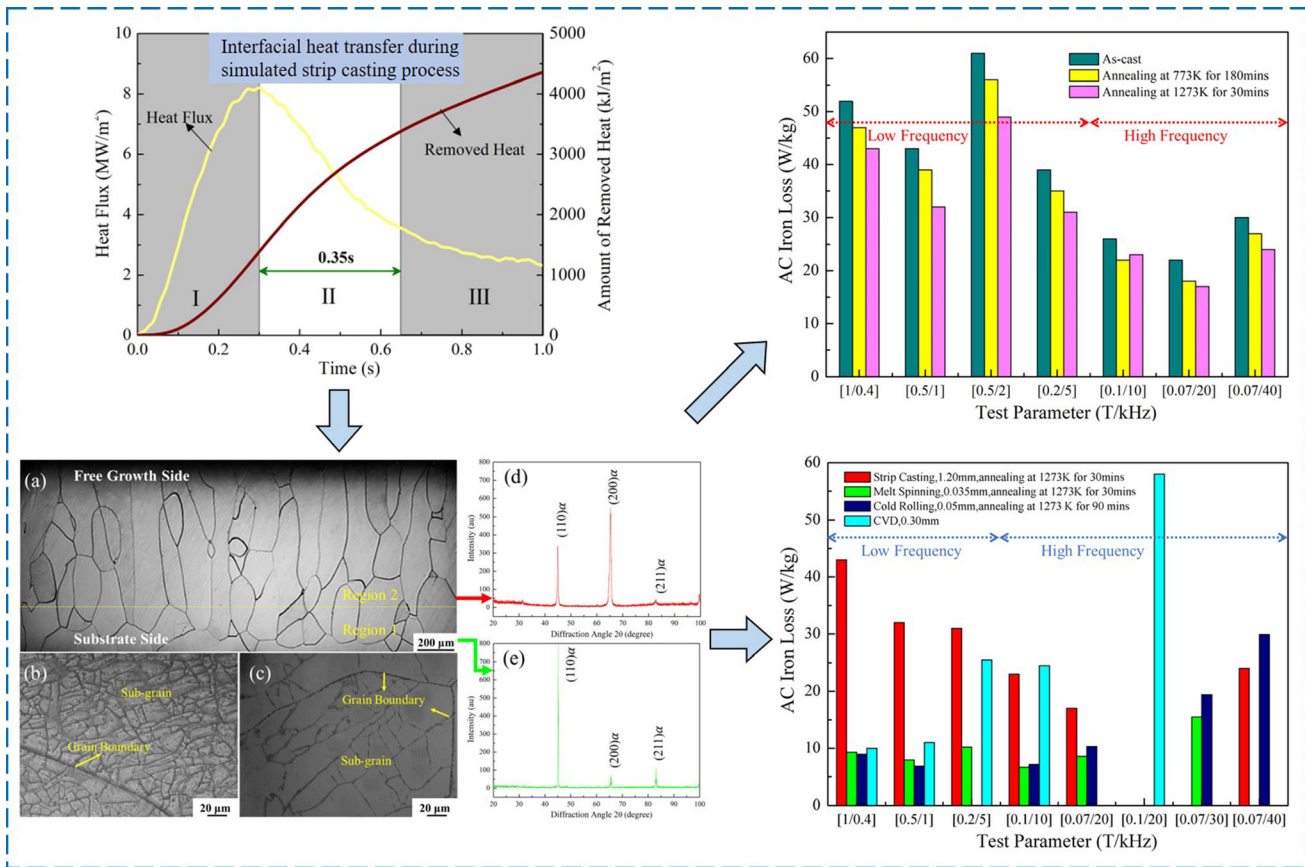
WANLIN WANG, HAIRUI QIAN, DAWEI CAI, LEJUN ZHOU, SONG MAO,
and PEISHENG LYU

An improved dip test apparatus was used to simulate the strip casting of 6.5 wt pct Si steel in this study. The results showed that the interfacial heat flux between melt and substrate could reach maximum value of 8.2 MW/m^2 , with $> 4350 \text{ kJ/m}^2$ heat being removed in the first 1.0 s. The as-cast strip mainly consisted of large columnar grains hundreds of microns in length. The high cooling rate of the as-cast strip suppressed the formation of ordered phases and the precipitation of elements. Only several complex particles of MnS-TiN of a few nanometers were found. After annealing at 1273 K (1000 °C) for 30 minutes, a large number of small particles such as TiN precipitated from the ferrite matrix. Within the testing frequency and magnetic field strength, the three strip samples obtained at different conditions showed the lowest iron loss at the frequency of 20 kHz and the magnetic field strength of 0.07 T, which were 22, 18 and 17 W/kg, respectively. The coercive force and iron loss decreased with increasing heat treatment temperature, while the magnetic permeability showed the opposite pattern. The magnetic permeability and iron loss of the silicon steel strip produced by strip casting are comparable to those of the silicon steel products produced by other techniques such as melt spinning and conventional rolling.

WANLIN WANG, HAIRUI QIAN, DAWEI CAI, LEJUN ZHOU, SONG MAO, and PEISHENG LYU are with the School of Metallurgy and Environment, Central South University, Changsha 410083, China and National Center for International Research of Clean Metallurgy, Central South University, Changsha 410083, China. Contact e-mail: lyu.peisheng@csu.edu.cn

Manuscript 7 September 2020; accepted 6 February 2021.

Article published online March 12, 2021



<https://doi.org/10.1007/s11661-021-06191-y>
 © The Minerals, Metals & Materials Society and ASM International 2021

I. INTRODUCTION

SILICON steels are important soft magnetic materials for the manufacturing of various motors and generator cores, and so on, which are widely used in the electronic, power, military and civil industries.^[1–3] The traditional manufacturing process of silicon steel sheets includes many complicated and rigorous procedures, which leads to high costs and high-energy consumption.^[4] Strip casting as an advanced near-net-shape casting technique allows directly casting liquid steel into an ultra-thin strip under sub-rapid solidification conditions, with the cooling rate magnitude of 10^2 K/s to 10^3 K/s (10^2 °C/s to 10^3 °C/s).^[5–7] Therefore, the strip casting technique has many advantages, such as energy saving, lower operating and investment costs and higher tolerance to impurities in the steel.^[8–11] Among all kinds of strip casting techniques, twin-roll casting (TRC) is the most mature and popular one. In addition, the strip casting technique could break through the limit of silicon content in the steel compared to the traditional casting method. The increasing silicon content in silicon steel could significantly reduce the core loss, and magnetostriction barely exists when the silicon content reaches 6.5 wt pct.^[12,13] Besides, during the strip casting

of silicon steels, the as-cast strip would preferentially form a $\langle 100 \rangle$ texture with coarse grains,^[14] which benefits the physical properties of final silicon steel sheets.

The cooling rate of molten metal has a great effect on the solidification microstructure during the casting process and thus affects the properties of the final metal products.^[15] Therefore, during the strip casting process, the interfacial heat transfer between the melt and roller, which determines the cooling rate of molten steel, would control the solidification microstructure of the as-cast strip and further influence properties of the final strip product. Additionally, the interfacial heat transfer also determines the productivity of the strip caster.^[16] As a result, many studies on the interfacial heat transfer between the melt and roller during the strip casting process have been carried out. Droplet ejection^[17–22] and dip test apparatus^[23–25] are two effective methods for studying the interfacial heat transfer pertinent to strip casting in the laboratory, through which molten steel solidifies in direct contact with the water-cooled copper substrate. Compared to the droplet ejection apparatus, the dip test apparatus is more reliable for obtaining the sub-rapid solidified steel strip. The dip test apparatus was first designed by Strezov^[23,24] to cast 304

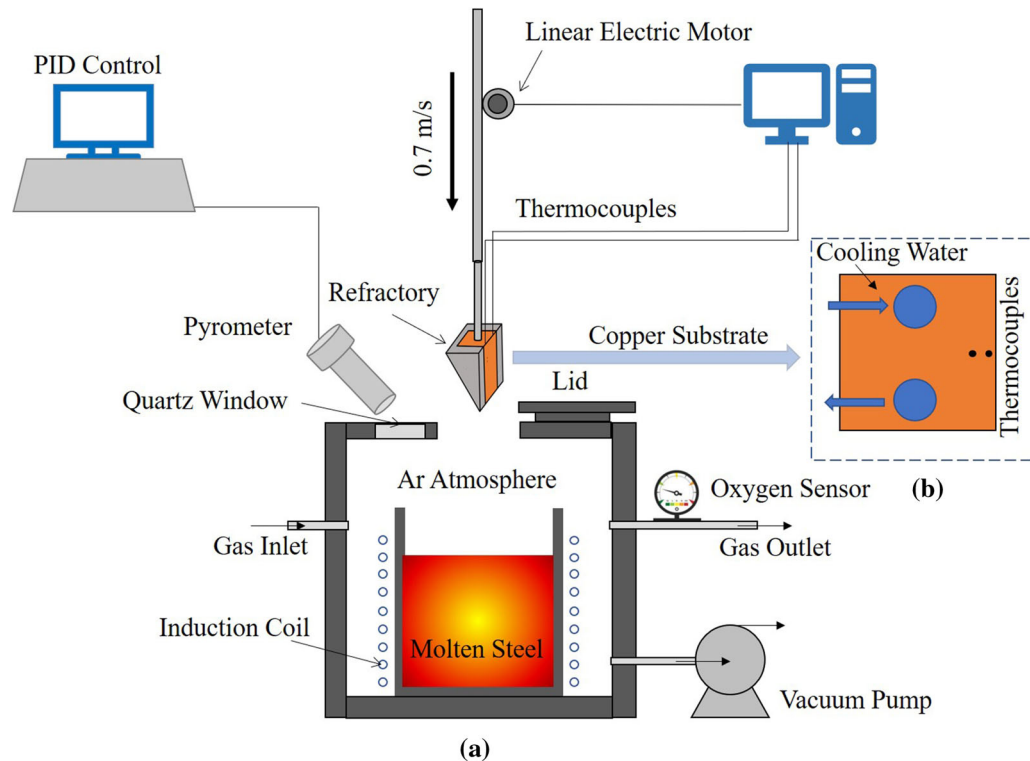


Fig. 1—(a) The schematic illustration of the dip test apparatus and (b) the top view of the copper substrate.

Table I. The Designed Composition of Experimental Silicon Steel (Wt Pct)

C	Si	Mn	Al	P	S	Ti	Fe
0.003	6.5	1.0	0.04	0.005	0.003	0.01	bal.

stainless steel strips with the aim of studying the effect of casting parameters on the interfacial heat transfer behavior. Wang *et al.*^[25] used the dip test apparatus to investigate the relationship among the deposited film, substrate roughness, solidification microstructure and interfacial heat transfer during the casting of the low-carbon martensitic steel strip.

The microstructure and second-phase precipitate are two important factors that affect the magnetic properties of silicon steels. For example, MnS and AlN are the common precipitates found in the silicon steel sheets, and these precipitates would provide strong a pinning force on the grain boundaries, leading to the inhibition of grain growth during the secondary recrystallization, and hinder the movement of domain walls, resulting in the deterioration of the magnetic properties of electrical steels.^[26–29] In addition, complex Ag-MnS and Ag-AlN precipitates were reported by Wan.^[30] Lu *et al.*^[31] produced a grain-oriented 6.5 wt pct Si steel strip with a laboratory twin-roll caster and found that fine equiaxed grains with random texture were obtained under a relatively low melt superheat. Xu^[32] used a pilot

twin-roll caster to investigate the effect of pre-annealing on the precipitation, microstructure and texture of a non-oriented 2.6 wt pct Si electrical steel strip.

Even though the industrial production of high-silicon electrical steel by the strip casting technique has not been achieved, many fundamental studies on 6.5 wt pct Si electrical steels have been conducted in a laboratory-scale or pilot twin-roll caster. However, it is costly and inconvenient to do such experiments; especially, it is extremely difficult to study the interfacial heat transfer between the melt and roller. The dip test apparatus has been demonstrated to be an ideal way to study the strip casting process. As for the studies on the relationship between microstructure and properties of the steel strip, Dorin *et al.*^[33,34] used a dip tester to study the second-phase precipitate and the mechanical properties of high-strength micro-alloy steel strips. Xiong *et al.*^[35–40] applied it to investigate the microstructure and mechanical properties of dual-phase (DP) and transformation-induced plasticity (TRIP) steel strips. However, studies on high-silicon electrical steel strips using the dip test apparatus have never been reported. In this article, the composition of a high-silicon electrical steel was designed, and an improved dip test apparatus was developed to cast the 6.5 wt pct Si electrical steel strip at a sub-rapid solidification rate with the aim to provide a comprehensive understanding of the interfacial heat transfer, solidification microstructure, precipitation and magnetic properties of the high-silicon electrical steel strip.

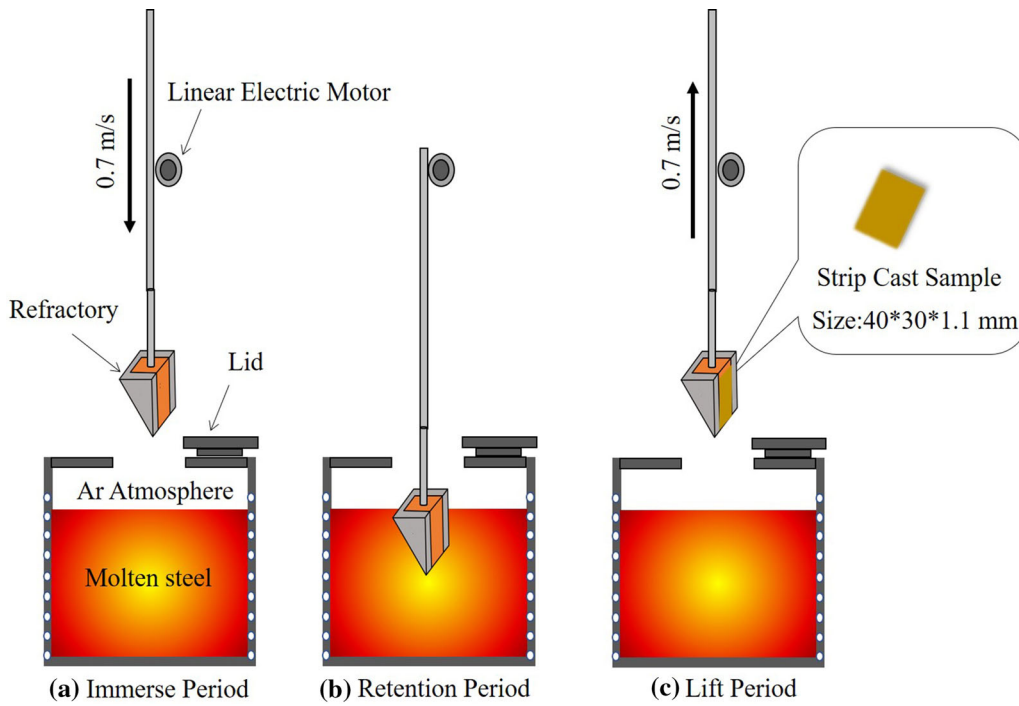


Fig. 2—Experimental process of the dip test apparatus.

II. MATERIALS AND EXPERIMENTAL METHODS

A. Experimental Apparatus and Preparation of Experimental Materials

The dip test apparatus is an effective simulator to study the initial contact between the melt and roller during the strip casting process, and an ideal size of the strip cast sample could be obtained under sub-rapid solidification conditions. Based on the previous success with a mold simulator,^[41,42] the dip test apparatus has been further developed by Steel Research Center at Central South University to investigate the relationship among the interfacial heat transfer, solidification structure and properties of a high-silicon steel strip. The schematic illustration of the improved dip test apparatus is shown in Figure 1, which mainly consists of four parts: atmosphere control, induction melting, substrate movement control and data acquisition. The atmosphere control part can achieve the oxygen partial pressure inside the furnace chamber by vacuuming and flowing high-purity argon gas (99.99 pct) through the shield furnace system during the tests (as shown in Figure 1(a)). The induction melting part has the function of melting the raw materials through a high-frequency induction furnace and controlling the molten steel at a certain superheat by the proportion-integration-differentiation (PID) control technique. The movement control part includes a copper substrate that can move downward through the linear electric motor. The copper substrate is designed as a wedge-shaped water-cooled substrate as shown in Figure 1, which could reduce the splash of molten steel. Three sides of the substrate were wrapped with refractory to ensure only

one effective contact area between the copper substrate and molten steel. The data acquisition system was used to collect the responding temperature histories of the copper substrate during the melt/substrate contact. The experimental raw materials include industrial pure iron, low-aluminum ferrosilicon and electrolytic manganese; the designed composition is shown in Table I, and its liquidus temperature is about 1753 K (1480 °C). The raw materials are polished by abrasive papers and then cleaned in ethanol by ultrasonic agitation prior to the dip test experiment.

B. Experimental Procedure

Figure 2 illustrates the experimental process of the dip test apparatus. Firstly, 5kg raw materials were charged into a magnesia crucible and the oxygen partial pressure inside furnace chamber was controlled at 2×10^{-20} atm. Then the raw materials were heated by a high-frequency induction furnace. Through PID control technique, the molten steel was hold at 1833 K (1560 °C) at a superheat of 80 K (80 °C). Next, the furnace lid was opened, and the inert gas curtain was turned on to prevent the air from entering the furnace chamber. Then, the water-cooled copper substrate was immersed into the molten steel at the speed of 0.7 m/s. After the retention period of 350 ms in the molten bath, the copper substrate was withdrawn to the original position. During the immersion test, the responding temperatures of substrate were measured by two highly sensitive K-type thermocouples, which were embedded inside the substrate with the distance of 1 mm and 3 mm horizontally away from the substrate hot surface, respectively. At the same time, the strip cast sample with the size of 40 mm (length) x 30

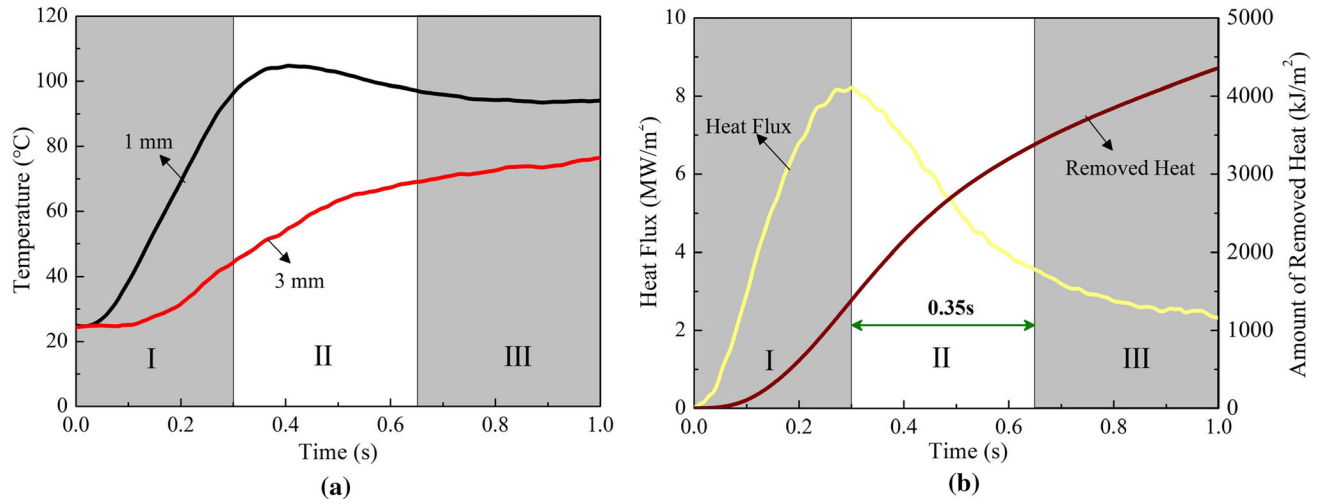


Fig. 3—(a) The responding temperatures measured by thermocouples and (b) the interfacial heat transfer between molten steel and substrate.

mm (width) x 1.1 mm (thickness) could be obtained and was cooled in the air. Besides, in order to study the effect of heat treatment on the microstructure and magnetic performance of silicon steel strips, the as-cast strip samples were annealed at 773 K (500 °C) for 180 minutes and 1273 K (1000 °C) for 30 minutes respectively by using an atmosphere-controlled furnace.

C. Analytical Methods

The inverse heat conduction problem (IHCP) mathematical model^[43-46] was used to calculate the heat flux across the substrate surface. In the IHCP model, the thermal conduction equation (Eq. 1) and boundary conditions (Eqs. 2 and 3) are expressed as:

$$c\rho \frac{\partial T}{\partial t} = \frac{\partial}{\partial x_i} \left(\lambda \frac{\partial T}{\partial x_i} \right), \quad x_i \in \Omega, \quad t \geq 0 \quad [1]$$

$$\lambda \frac{\partial T}{\partial x_i} \Big|_{x_i=0} = q \quad [2]$$

$$T|_{x_i=d} = T_s \quad [3]$$

where c is the specific heat capacity in J/K kg, ρ is the density in kg/m³, T represents the temperature in K, t is time in seconds, T stands for thermal conductivity in W/m K, x_i is the position in meters, Ω means the one-dimensional calculation domain in the range from 0 to 3 mm, q is the heat flux across the substrate surface, d is the position and equals 3 mm, and T_s is the substrate temperature measured by the thermocouple, which is 3 mm away from the substrate surface. In this article, Beck's nonlinear estimation method^[43, 44] was used to solve the IHCP model, which can improve the convergence speed and reduce the calculation amount of the IHCP solution.

The microstructure of strip cast samples was observed by an optical microscope (OM, Leica DM4000M). X-ray diffraction (XRD, Advance D8) was used to identify the

phase composition of the strip cast samples. Electron probe microanalysis (EPMA, JXA-8530F) was used to analyze the element distribution of strip cast samples. A scanning electron microscope (SEM, JSM-6360LV) was used to observe the second-phase particles in the samples. To further study the precipitation behavior and microstructure, a transmission electron microscope (TEM, Tecnai G2 F20) was applied. The TEM samples were prepared by using a double-jet polishing apparatus in a solution containing 10 vol pct perchloric acid and 90 vol pct ethanol at the temperature of 253 K (-20 °C). A vibrating sample magnetometer (VSM, PPMS-9) was used to determine the direct current (DC) performance and alternating current (AC) iron loss of the silicon steel strips, and the tested samples were of 1.1 mm x 2.0 mm x 2.0 mm size.

III. RESULTS

A. Interfacial Heat Transfer and Microstructure

With the help of highly sensitive thermocouples and the IHCP model, the real-time interfacial heat transfer behavior during strip casting could be measured and calculated, which was plotted vs time, as shown in Figure 3. Figure 3(a) shows that the responding temperature 1 mm away from the hot surface rises quickly during the downward movement period in stage I, as the substrate is heated consecutively when it starts to contact with the high-temperature molten steel. The substrate reaches the target position at 0.3 s in stage I and then is held in the bath for 350 ms as shown in stage II. The responding temperature (1 mm) picks the maximum value in stage II because of the continuous heating and then starts to decrease. This could be explained as the cooling potential of the substrate is higher than the heating potential of the high-temperature solidified strip because of the increasing thermal resistance between the substrate and solidified strip, caused by the growth of the solidified strip cast and the

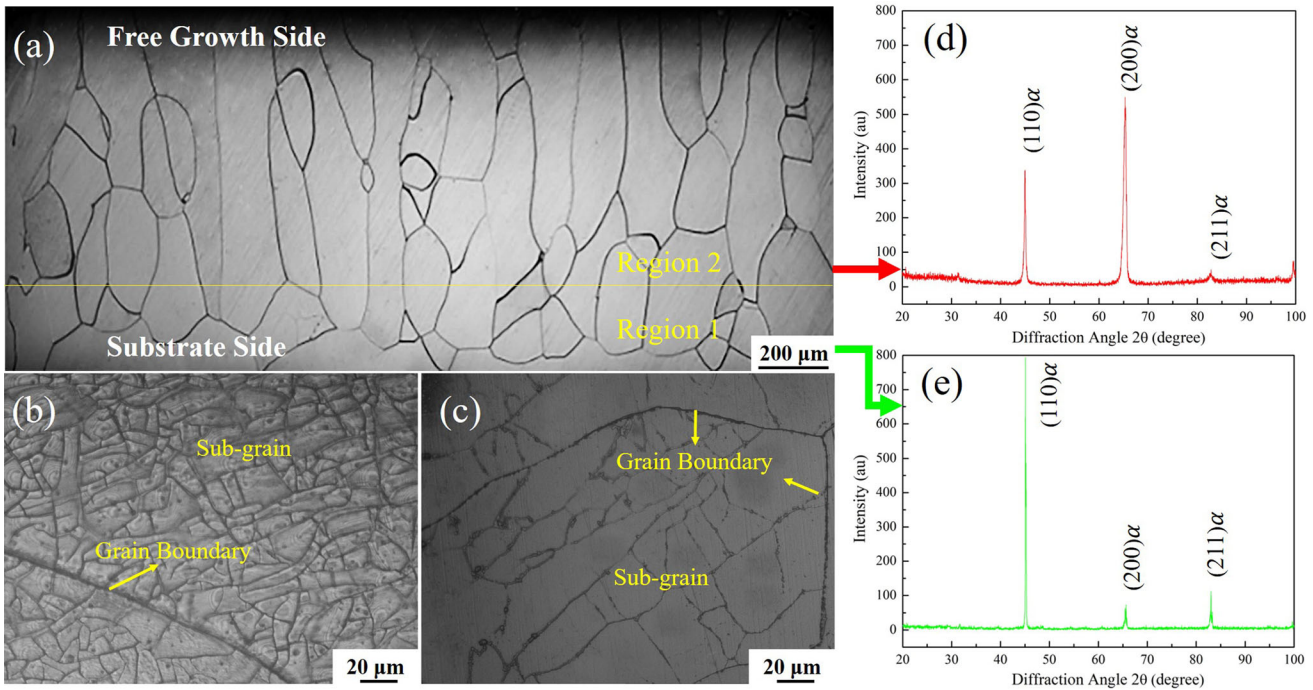


Fig. 4—(a) Microstructure of the as-cast strip, (b, c) sub-grain morphology of the as-cast strip and the heat-treated strip annealed at 1273 K (1000 °C) for 30 min, and (d, e) XRD analysis for the bottom surface of region 2 and region 1.

formation of air gap between the strip cast and substrate. Finally, the temperature becomes stable when the substrate is withdrawn out of the bath (0.65 to 1.0 seconds) because of the heat balance between the high-temperature strip cast and cooling water. Figure 3(b) shows the interfacial heat flux between the melt and substrate and the total heat removed by the water-cooled substrate during the immersion test. This indicates that the variation of interfacial heat flux has a similar pattern to that of the responding temperatures, and the heat flux reaches the maximum value of 8.2 MW/m² at the time of 0.3 seconds and then attenuates quickly to 3.5 MW/m² during the retention period (from 0.3 to 0.65 seconds) because of the increasing interfacial thermal resistance between the strip cast and substrate. The total amount of removed heat is about 4350 kJ/m² during the testing time of 1.0 seconds. For the traditional continuous casting, the average in-mold interfacial heat flux usually ranges from 1 to 3 MW/m², while it could reach 6 to 15 MW/m² in a twin-roll strip caster.^[10,47] The variation and magnitude of the interfacial heat flux for the dip test (Figure 3) are similar to those occurring in an industrial strip caster, which confirms the reliability of the current study.

Microstructures of the strip samples are shown in Figure 4. Figure 4(a) is the microstructure etched by 4 pct Nital, where the bottom part is close to the copper substrate and the other side is the free growth face. The general microstructure of the silicon steel strip consists of dominant large-size columnar grains with different ratios of length to width and a very thin layer of fine

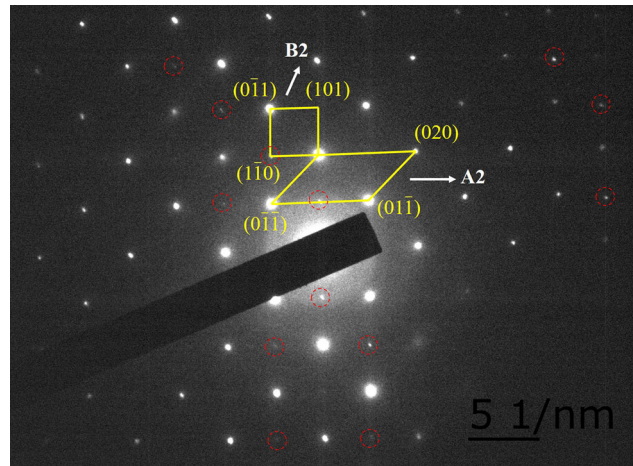


Fig. 5—SAED of the zone axis of [100] for the as-cast silicon steel strip. The dotted circles indicate superlattice diffraction spots of B2 ordered phase.

equiaxed grains, as shown in Figure 4(a), where most of the fine equiaxed grains are close to the substrate. With the proceeding of the solidification process, it can be observed that the large-size columnar grains grow along the heat transfer direction, which is perpendicular to the substrate surface. The size of coarse columnar grains is around 600 to 1000 μm in length and 100 to 200 μm in width. When the as-cast sample was deeply etched by the saturated picric acid in a 343 K (70 °C) water bath, a large amount of polygonal subgrains < 30 μm in size inside the ferrite columnar grain could be found, as

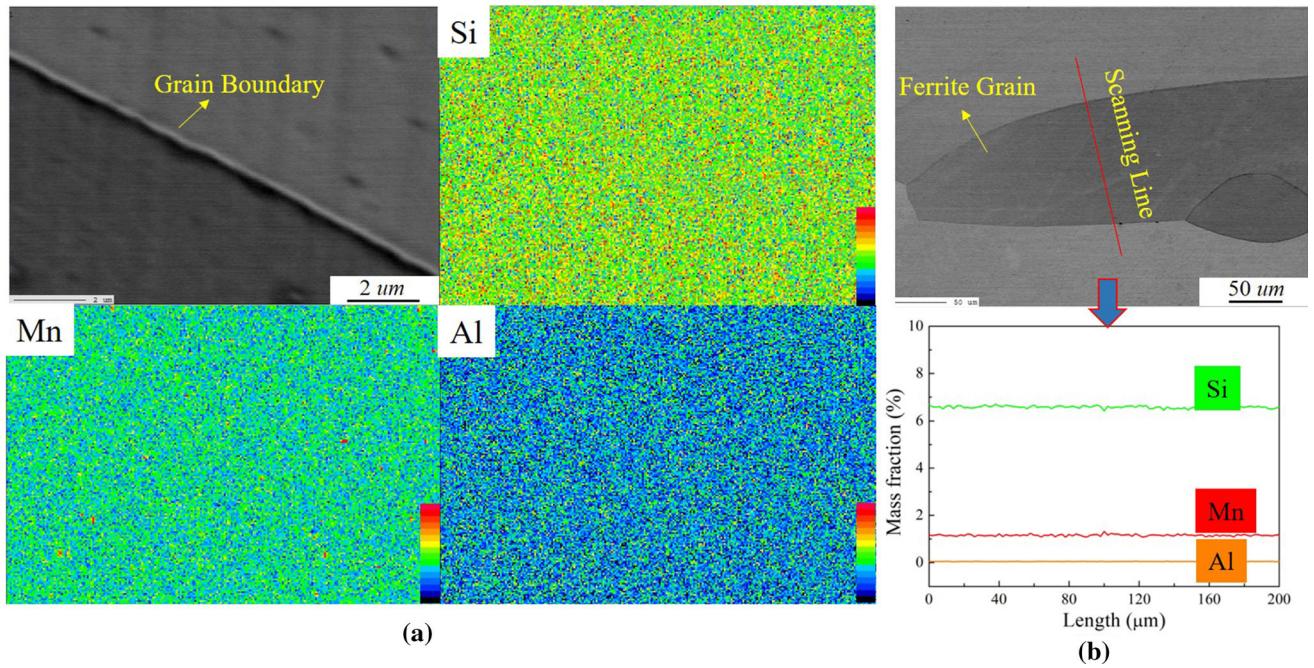


Fig. 6—Electron probe microanalysis of the as-cast strip sample: (a) element mapping around the grain boundary and (b) line scanning analysis through one ferrite grain.

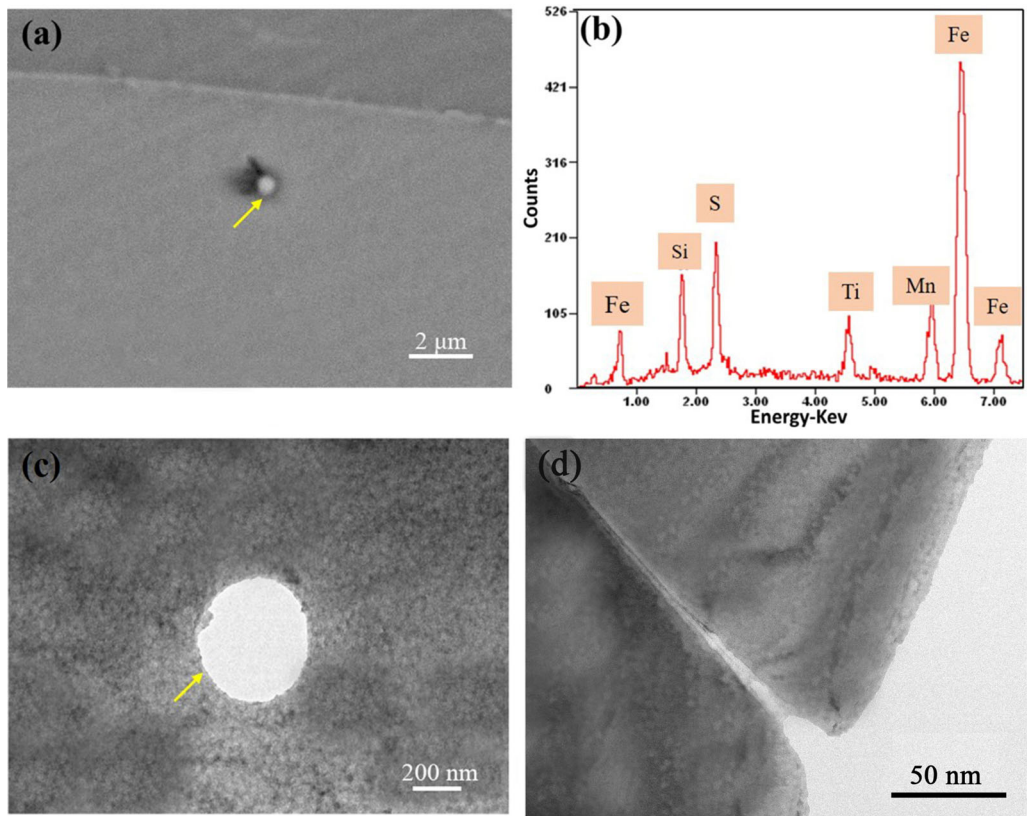


Fig. 7—SEM and TEM micrographs of particles in the as-cast strip sample: (a) the complex particle in the as-cast strip by SEM, (b) EDS spectrum of the particle by SEM, (c) the complex particle in the as-cast strip by TEM and (d) typical TEM micrograph without any precipitation of tiny particles in the as-cast strip. Yellow arrows indicate second-phase particles.

shown in Figure 4(b). However, in Figure 4(c) shows that the subgrain size of the steel strip becomes coarser after annealing treatment at 1273 K (1000 °C) for 30 minutes.

Figures 4(d) and (e) shows the XRD analysis results for the bottom part (parallel to the substrate face) of region 2 and region 1 in the strip cast sample. According to the Fe-Si binary phase diagram,^[48] 6.5 wt pct Si steel is constituted of B2 and DO3 ordered phases at equilibrium condition. For the as-cast strip obtained in this study, neither diffraction peaks of DO3 nor B2 ordered phases have been found in the XRD patterns, indicating that the 6.5 wt pct Si steel strip is mainly composed of α -ferrite phase (A2 disordered phase) and the formation of ordered phases is suppressed significantly. However, the presence of ordered phases in the as-cast strip cannot be completely ruled out because a small volume fraction of ordered phases is hardly detected by XRD. From Figures 4 (d) and (e), it is obvious that the peak intensities of (110) α and (200) α

for region 1 are significantly different from that for region 2. The reason for the difference of diffraction intensity can be attributed to the directional growth of ferrite columnar grains in region 2, which corresponds to the increasing of peak intensity of (200) α .

As shown in Figure 5, selected area electron diffraction (SAED) was conducted for the as-cast silicon steel strip by TEM, and the evident diffraction spots of A2 disordered phase can be observed, suggesting that the dominant structure of the as-cast strip is α -ferrite phase. Besides, a weak superlattice diffraction spot can also be found in the diffraction pattern, which corresponds to the B2 ordered phase according to its Miller indexes. The electron diffraction pattern in Figure 5 shows that the as-cast strip is mainly composed of α -ferrite phase with a small volume fraction of B2 ordered phases, further indicating that the formation of ordered phases in the as-cast 6.5 wt pct Si steel produced by the dip test apparatus was suppressed. The existence of ordered phases would increase the brittleness of silicon steel, and

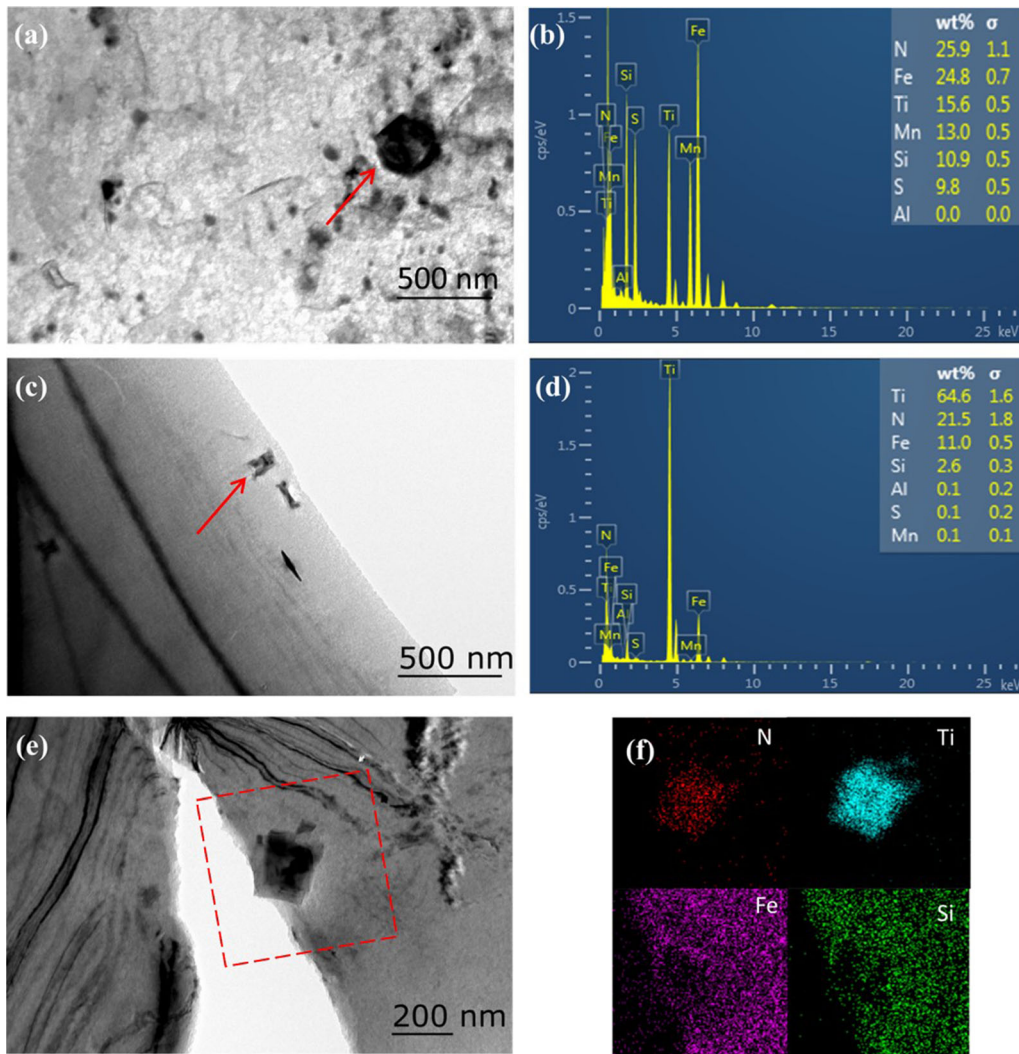


Fig. 8—TEM observation of particles in the as-cast strip sample after heat treatment at 1273 K (1000 °C) for 30 min: (a) the MnS-TiN complex particle and small round-shaped particles in the heat-treated strip, (b) EDS analysis of the particle indicated by the red arrow in (a), (c) the individual TiN particle in the heat-treated cast, (d) EDS spectrum of the particle indicated by the red arrow in (c), (e) the selected TiN particle for EDS mapping analysis and (f) the mapping analysis result of the area indicated by the red dotted box in (e).

therefore the suppression of ordered phases by the high cooling rate during strip casting would improve the processability of high-silicon steel strip.

To investigate the distribution behavior of alloy elements in the strip cast, EPMA was conducted, and the results are shown in Figure 6(a). The results suggest that there is no segregation of Si, Mn and Al elements inside the grain and around the grain boundary, and these alloying elements are well dispersed in the ferrite matrix as solutes or tiny precipitated particles. Since the presence of tiny precipitated particles is beyond the resolution of EPMA, the TEM analysis is conducted in Section III-B. The EPMA line scanning is also performed across one grain range, as shown in Figure 6(b), where the content of alloy elements Si, Mn and Al are maintained at about 6.5 wt pct, 1.0 wt pct and 0.04 wt pct, respectively, over the distance of 200 μm , confirming the uniform distribution of the elements in the strip cast.

B. Precipitation of Second-Phase Particles

The morphology of second-phase particles in the as-cast strip was characterized by SEM and TEM. As shown in Figure 7(a), a round-shaped particle with a diameter of about 350 nm is found in the as-cast strip by SEM, which may contain elements of Mn, S, Ti, and so on, according to the energy dispersive spectrum (EDS) analysis (Figure 7(b)). This type of round-shaped particle with complex chemical compositions was also observed by TEM, as shown in Figure 7(c). However, there is no evidence of precipitation of other small-sized particles in the as-cast strip from Figure 7(d) except for the very few above-mentioned round-shaped particles, which may be MnS-TiN or MnS-TiO₂ complex particles.

The precipitation behavior of the strip sample annealed at 1273 K (1000 °C) for 30 minutes was also investigated. As shown in Figure 8(a), the round-shaped particle with a diameter of about 300 nm was found in the heat-treated strip, and the EDS analysis (Figure 8(b)) indicated that it was the MnS-TiN complex particle, which was also found in the as-cast strip.

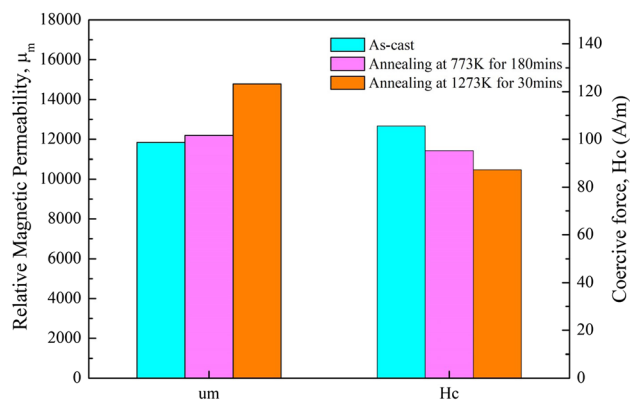


Fig. 9—Magnetic permeability and coercive force of the as-cast and heat-treated strips.

Besides, many small round-shaped particles with the diameter < 100 nm were found and distributed uniformly after the heat treatment of the cast sample, as shown in Figure 8(a). In addition to the small round-shaped particles, small rectangular or square particles with a length of 50 nm to 200 nm also could be found in the strip after the heat treatment, as shown in Figure 8(c). The EDS analysis (Figure 8(d)) shows that these particles are independent TiN particles, even though there is low Ti content in the studied steel. The EDS mapping analysis (Figures 8(e) and (f)) confirms again that independent TiN would form after the heat treatment. Obviously, the MnS-TiN complex particle with a diameter > 300 nm would form during the sub-rapid solidification of molten steel for both the as-cast and the heat-treated strips. Dorin *et al.*^[34,49] also found the formation of MnS-containing particles in both Cu-bearing steel strips and high-strength low-alloy steel strips produced by the simulated strip-casting process without heat treatment, but the particles only contain Mn and S, and their size is < 100 nm.

C. Magnetic Performance of Silicon Steel Strips

The direct current (DC) performance of the strip samples obtained at different conditions was measured by vibrating sample magnetometer (VSM), and the results are shown in Figure 9, where the coercive force (H_c) is 105.6 A/m for the as-cast strip, and it reduces to 95.2 A/m for the strip annealed at 773 K (500 °C) for 180 minutes and to 87.3 A/m for the strip annealed at 1273 K (1000 °C) for 30 minutes. The relative magnetic permeability of the as-cast strip is 11836, and it increases to 12198 and 14794, respectively, after the heat treatments of 773 K (500 °C) for 180 minutes and 1273 K (1000 °C) for 30 minutes. Figure 10 shows the results of alternating current (AC) iron loss analysis, where the iron loss reaches the lowest values of 22, 18 and 17 W/kg, respectively, for above three samples at the high frequency of 20 kHz and the magnetic field strength of 0.07 T, indicating that these silicon strip samples have a

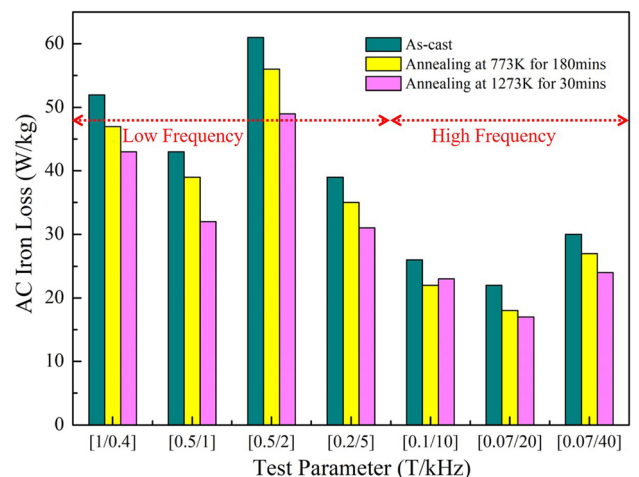


Fig. 10—AC iron loss of the silicon steel strips under different magnetic field strengths and frequencies.

better magnetic performance at high frequency under suitable magnetic field strength. Obviously, the test results suggest that the coercive force and iron loss decrease with the increasing of heat treatment temperature, and the relative magnetic permeability shows the opposite pattern.

IV. DISCUSSION

A. Microstructure Evolution and Precipitation Behavior

The rapid solidification corresponding to the peak heat flux in Figure 3(b) during the initial melt/substrate contact causes higher undercooling, which contributes to the high nucleation rate and therefore the formation of the fine equiaxed grains at the subsurface of the as-cast strip (Figure 4(a)). With the decreasing of interfacial heat flux between the substrate and melt, the relatively slow solidification results in the directional solidification perpendicular to the substrate surface and large-size columnar grains (Figure 4(a)). A large number of polygonal sub-grains inside the ferrite columnar grain of the as-cast strip (Figure 4(b)) is caused by the non-equilibrium solidification of the molten steel during the strip casting process. After annealing at 1273 K (1000 °C) for 30 minutes, the subgrain size of the silicon steel strip gets coarsened (Figure 4(c)), resulting in fewer sub-grain boundaries of the heat-treated strip compared to the as-cast strip. It is known that the sub-grain boundary belongs to a small angle boundary characterized by many dislocations. Therefore, it can be concluded that the dislocation density of the as-cast strip is higher than that of the heat-treated strip. The reduction of the dislocation density of the heat-treated strip was because the dislocations in the crystal lattice would slip and merge into each other at a high temperature of 1273 K (1000 °C). The high-density dislocation was also found in the as-cast strip of high-strength low-alloy steel by Dorin.^[50]

Compared with the low cooling rate during the traditional continuous casting process, the high cooling rate during the strip casting process suppresses the formation of ordered phases and influences the precipitation behavior of alloy elements. Combining the TEM observation with the EPMA results suggests that the segregation and precipitation of alloy elements in the

as-cast silicon strip were effectively inhibited, and most of them were well dispersed in the ferrite matrix as solutes except for very few particles of MnS-TiN. This is because the alloying elements do not have enough time to segregate or precipitate at such a high cooling rate when the strip solidifies from liquid to solid. It has been reported that MnS would precipitate on the high melting particles that act as nucleants in the molten steel.^[51] Therefore, concerning the formation mechanism of the MnS-TiN complex particle in this study, it is assumed that TiN particles first precipitate from liquid steel before the precipitation of MnS and then MnS nucleates and grows on the surface of the precipitated TiN particle. After the heat treatment at the temperature of 1273 K (1000 °C) for 30 minutes, the as-cast strip, which is supersaturated with alloy elements, will move to the equilibrium state, and thus the supersaturated alloy elements will precipitate from the supersaturated solid solution to form smaller particles like TiN with the diameters < 200 nm. These small particles will produce an effective pinning force on the grain boundary to restrain the growth of the grain and will also improve the strength of the silicon steel strip.

B. Effect of Heat Treatment on the Magnetic Properties of Silicon Steel Strips

It is well known that the existence of dislocations in the crystal lattice will introduce stress field, which can hinder the movement of the magnetic domain and thus deteriorate the DC magnetic performance, *i.e.*, increase the coercive force and decrease the magnetic permeability. As discussed before, the subgrains will coarsen (Figure 4(c)) and the dislocation density will reduce for the strip cast sample experiencing the annealing process, contributing to the improvement of the DC magnetic performance. On the other hand, the ferrite grains of the high-silicon steel strip will grow further during the annealing process and the coarse grains will reduce the grain boundary, which will improve the movement of the magnetic domain and thus improve the DC magnetic performance of the steel strip. Consequently, the coercive force decreases and magnetic permeability increases for the steel strip after heat treatment at 773 K (500 °C) and 1273 K (1000 °C), as shown in Figure 9.

Table II. Comparison of the Relative Magnetic Permeability of the Strip Samples With That of the 6.5 Wt Pct Si Steel Products Produced by Other Techniques

Technique	Final Treatment	Thickness (mm)	Magnetic Permeability
Simulated Strip Casting	as-cast	1.10	11836
	annealing at 1273 K (1000 °C) for 30 min	1.10	14794
Melt Spinning ^[52]	as-spun	0.035	1843
	annealing at 1273 K (1000 °C) for 30 min	0.035	13769
Conventional Rolling ^[53]	cold rolling + annealing at 1273 K (1000 °C) for 90 min	0.050	11200
	cold rolling + annealing at 1473 K (1200 °C) for 90 min	0.050	25000
Spray Forming ^[54]	as-sprayed	> 0.70	8250
	cold rolling + annealing at 973 K (700 °C) for 60 min	0.60	8870

Although many small second-phase particles, which also can hinder the movement of magnetic domain and deteriorate DC magnetic performance, precipitated from the ferrite matrix after the annealing treatment (Figure 8), Figure 9 suggests that the influence of precipitated particles on the DC magnetic performance is negligible compared to the dislocation density and grain size. When annealing treatment was performed at a relatively low temperature (773 K [500 °C]), the mobility of the dislocations and the growth of the ferrite grains were limited, which could not significantly reduce the dislocation density and coarsen the grains of the strip sample. Even though the annealing time at 1273 K (1000 °C) (30 minutes) is much shorter than that at 773 K (500 °C) (180 minutes), the reduction of dislocation density and the growth of the grains are more significant for the heat-treated sample annealed at 1273 K (1000 °C) because of the high thermally driven force. Therefore, the sample treated at a high annealing temperature (1273 K [1000 °C]) shows a better DC magnetic performance, as shown in Figure 9.

C. Comparison With the Magnetic Permeability and Iron Loss of 6.5 Wt Pct Si Steel Products Produced by Other Techniques

Table II compares the relative magnetic permeability of the strip samples with that of 6.5 wt pct Si steel products produced by other techniques. It is shown that the magnetic permeability of the strip samples obtained by strip casting in this study are comparable to that of silicon steel products produced by other techniques. It is noteworthy that the magnetic permeability of the ribbon produced by melt spinning increases about five times after the annealing treatment at 1373 K (1100 °C) for 90 minutes, because the grain size of the ribbon produced by melt spinning increases more than ten times after the annealing treatment at 1373 K (1100 °C) for 90 minutes (from a few microns to about 30 microns),^[52] which reduces the grain boundary dramatically and thus

improve the DC magnetic performance. However, the increment of the magnetic permeability of the strip sample after the same heat treatment is not as significant as the ribbon produced by melt spinning. This is because the growth of grains is limited even at high annealing temperature when the initial grain size of the sample is big enough ($> 100 \mu\text{m}$). Additionally, the precipitation of the small particles from the studied silicon steel at 1273 K (1000 °C) would introduce an effective pinning force on the grain boundary to restrain the growth of the grain.

Hysteresis loss and the eddy current loss are the two primary components of the total iron loss. It is known that the hysteresis loss would be dominant at low frequency; however, the eddy current loss would become significant at high frequency.^[53] After the annealing treatment, the decreasing of the dislocation density and the increasing of ferrite grain size of the heat-treated strip samples would enhance the movement of magnetic domain and thereby reduce the hysteresis loss. Consequently, as can be seen in Figure 10, the total AC iron loss of the strip cast after heat treatment would attenuate throughout the test frequency from 0.4 to 40 kHz, especially within the low frequency range (< 10 kHz). It could be found that the iron loss of the heat-treated strips is still lower than that of the as-cast strip at high frequency, which is different from the result reported by Liang^[52] in which the iron loss of the heat-treated silicon steel ribbons is higher than that of the ribbons without heat treatment at high frequency because of the higher eddy current loss of the heat-treated ribbons. The above difference could be explained by the large number of small particles found in the heat-treated strip increasing the electrical resistance, which could reduce the eddy current loss of the strip significantly at high frequency.

Figure 11 compares the AC iron loss of the heat-treated steel strip with that of the 6.5 wt pct Si steel products produced by other techniques. It can be observed that the iron loss of the silicon steel strip in this study at low frequency (< 10 kHz) is higher than that of the others, and the silicon steel ribbon produced by the melt spinning technique exhibits lower iron loss at both low and high frequencies. However, it is difficult for the melt spinning technique to achieve large-scale industrial production because of its low capacity. It is noteworthy that the iron loss of the silicon steel strip at high frequency (> 10 kHz) is comparable to that of the others. In particular, the iron loss of the heat-treated strip at high frequency is lower than that of the silicon steel produced by chemical vapor deposition (CVD), and the iron loss of the heat-treated strip at the frequency of 40 kHz is lower than that of the conventional cold rolling strip. Therefore, it is indicated that the silicon strip produced by strip casting shows great potential to be used in the high-frequency environment. In addition, further treatments such as rolling are necessary for reducing the microstructural defects and porosity, which contribute to the reduction in the AC iron loss of the strip at low frequency.

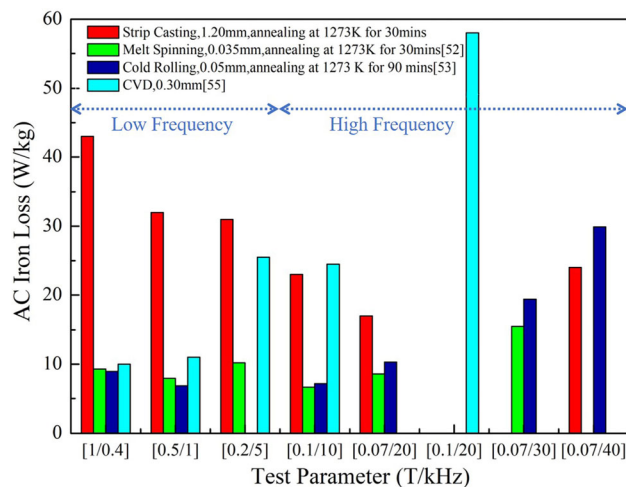


Fig. 11—Comparison of the AC iron loss of the heat-treated steel strip with that of the 6.5 wt pct Si steel products produced by melt spinning, cold rolling and CVD.

V. CONCLUSION

The simulation of strip casting to manufacture 6.5 wt pct Si steel strips *via* the dip test apparatus was carried out for the first time to our knowledge. Interfacial heat transfer, microstructure, precipitation and magnetic performance of the strip cast under different annealing treatments were investigated in this article. The main conclusions are summarized as follows:

1. During strip casting, the variation of interfacial heat flux between the substrate and molten steel showed a similar pattern to that of the responding temperatures inside the substrate. The heat flux reached the maximum value of 8.2 MW/m² and then attenuated quickly to 3.5 MW/m² because of the increasing interfacial thermal resistance between the strip cast and substrate. In addition, the variation and magnitude of the interfacial heat flux are similar to those for an industrial strip caster, which confirms the reliability of the simulation study by the dip test apparatus.
2. The microstructure of the as-cast silicon steel strip was observed to be a mixture of dominant large-size columnar grains and a very thin layer of fine equiaxed grains. The high cooling rate during strip casting inhibited the formation of ordered phases and the precipitation of elements. Only several complex particles of MnS-TiN with a size of around 350 nm in diameter were found in the as-cast strip, but no smaller second-phase particles were observed. After annealing treatment at 1273 K (1000 °C) for 30 minutes, the dislocation density of the steel strip reduced, and many small-sized second-phase particles such as independent TiN precipitated from the ferrite matrix.
3. With the increasing of heat treatment temperature, the DC magnetic performance of the steel strip improved gradually. The coercive force (H_c) is 105.6 A/m for the as-cast strip, and it reduces to 95.2 A/m for the strip annealed at 773 K (500 °C) and to 87.3 A/m for the strip annealed at 1273 K (1000 °C). The relative magnetic permeability of the as-cast strip is 11836, and it increases to 12198 and 14794, respectively, after annealing treatment at the temperatures of 773 K (500 °C) and 1273 K (1000 °C).
4. After annealing treatment, the total AC iron loss of the silicon steel strip decreased within the test frequency from 0.4 to 40 kHz, especially for the low frequency (< 10 kHz). Within the testing frequency and magnetic field strength, the three strip samples obtained at different conditions showed the lowest iron loss at the high frequency of 20 kHz and the magnetic field strength of 0.07 T, which were 22, 18 and 17 W/kg, respectively, which shows that the silicon steel strips produced by strip casting have a better magnetic performance at high frequency under a suitable magnetic field strength.
5. The DC magnetic properties and iron loss at high frequency (> 10 kHz) of the silicon steel strip in this study are comparable to those silicon steel products

produced by the methods of melt spinning, conventional rolling, spray forming and CVD. Therefore, it is promising to apply the silicon strip produced by the strip casting technique in the high-frequency environment.

ACKNOWLEDGMENTS

The financial support from National Natural Science Foundation of China (U1760202) and Hunan Scientific Technology Project (2018RS3022, 2018WK2051) are great acknowledged.

REFERENCES

1. M. Takashima, M. Komatsubara, and N. Morito: *ISIJ Int.*, 1997, vol. 37, pp. 1263–68.
2. Z.S. Xia, Y.L. Kang, and Q.L. Wang: *J. Magn. Magn. Mater.*, 2008, vol. 320, pp. 3229–33.
3. N. Takahashi, Y. Suga, and H. Kobayashi: *J. Magn. Magn. Mater.*, 1996, vol. 160, pp. 98–101.
4. I. Tanaka and H. Yashiki: *IEEE Trans. Magn.*, 2010, vol. 46, pp. 290–93.
5. P.G.Q. Netto, R.P. Tavares, M. Isac, and R.I.L. Guthrie: *ISIJ Int.*, 2007, vol. 41, pp. 1340–49.
6. E.E.M. Luiten and K. Blok: *Energy Policy*, 2003, vol. 31, pp. 1339–56.
7. C.Q. Wang, Y.Y.Y. Fang, T.J. Li, and T.J. Li: *J. Iron Steel Res. (in Chinese)*, 2005, vol. 17, pp. 11–15.
8. S. Ge, M. Isac, and R.I.L. Guthrie: *ISIJ Int.*, 2012, vol. 52, pp. 2109–22.
9. N. Zapuskalov: *ISIJ Int.*, 2003, vol. 43, pp. 1115–27.
10. S. Ge, M. Isac, and R.I.L. Guthrie: *ISIJ Int.*, 2013, vol. 53, pp. 729–42.
11. R. Wechsler: *Scand. J. Metall.*, 2003, vol. 32, pp. 58–63.
12. J.Y. Park, K.H. Oh, and H.Y. Ra: *Scr. Mater.*, 1999, vol. 40, pp. 881–85.
13. H. Honma, Y. Ushigami, and Y. Suga: *J. Appl. Phys.*, 1991, vol. 70, pp. 6259–61.
14. Y.Q. Wang, X.M. Zhang, Z. He, G.Q. Zu, G.F. Ji, J.Y. Duan, and R.D.K. Misra: *Mater. Sci. Eng. A*, 2017, vol. 703, pp. 340–47.
15. W. Kurz and D.J. Fisher: *Fundamentals of Solidification*, Trans. Tech. Publications, Lausanne, 1998.
16. P. Noll and A.W. Cramb: *Iron Steel Technol.*, 2006, vol. 3, pp. 169–78.
17. P. Noll and A.W. Cramb: *Metall. Mater. Trans. B*, 2008, vol. 39, pp. 56–65.
18. P. Noll and A.W. Cramb: *ISIJ Int.*, 2007, vol. 47, pp. 1284–93.
19. C.Y. Zhu, W.L. Wang, and C. Lu: *J. Alloys Compd.*, 2019, vol. 770, pp. 631–39.
20. W.L. Wang, C.Y. Zhu, C. Lu, J. Yu, and L.J. Zhou: *Metall. Mater. Trans. A*, 2018, vol. 49, pp. 5524–34.
21. C. Lu, W.L. Wang, J. Zeng, C.Y. Zhu, and J. Chang: *Metall. Mater. Trans. B*, 2019, vol. 50, pp. 77–85.
22. C.Y. Zhu, W.L. Wang, J. Zeng, C. Lu, L.J. Zhou, and J. Chang: *ISIJ Int.*, 2019, vol. 59, pp. 880–88.
23. L. Strezov and J. Herbertson: *ISIJ Int.*, 1998, vol. 38, pp. 959–66.
24. L. Strezov, J. Herbertson, and G.R. Belton: *Metall. Mater. Trans. B*, 2000, vol. 31B, pp. 1023–30.
25. P.S. Lyu, W.L. Wang, H.R. Qian, J.C. Wu, and Y. Fang: *JOM*, 2020, vol. 72, pp. 1910–19.
26. K. Jenkins and M. Lindenmo: *J. Magn. Magn. Mater.*, 2008, vol. 320, pp. 2423–29.
27. K. Iwayama and T. Haratani: *J. Magn. Magn. Mater.*, 1980, vol. 19, pp. 15–17.
28. S. Mishra and V. Kumar: *Mater. Sci. Eng. B*, 1995, vol. 32, pp. 177–84.

29. Y. Wan, K.K. Feng, Q.Q. Zhao, Y.C. Wu, D.D. Fan, Y.J. Xia, J. Li, and Y.H. Wen: *Mater. Res. Express*, 2019, vol. 6, p. 1165.
30. Y. Wan, W. Chen, and Q. Zhao: *ISIJ Int.*, 2016, vol. 56, pp. 661–68.
31. X. Lu, F. Fang, Y.X. Zhang, Y. Wang, G. Yuan, Y.B. Xu, G.M. Cao, R.D.K. Misra, and G.D. Wang: *Mater. Charact.*, 2017, vol. 126, pp. 125–34.
32. Y.B. Xu, H.T. Jiao, Y.X. Zhang, F. Fang, X. Lu, Y. Wang, G.M. Cao, C.G. Li, and R.D.K. Misra: *J. Mater. Sci. Technol.*, 2017, vol. 33, pp. 1465–74.
33. T. Dorin, K. Wood, A. Taylor, P. Hodgson, and N. Stanford: *Acta Mater.*, 2016, vol. 115, pp. 167–77.
34. T. Dorin, K. Wood, A. Taylor, P. Hodgson, and N. Stanford: *Mater. Charact.*, 2016, vol. 112, pp. 259–68.
35. Z.P. Xiong, A.A. Saleh, A.G. Kostryzhev, and E.V. Pereloma: *J. Alloys Compd.*, 2017, vol. 721, pp. 291–306.
36. Z.P. Xiong, A.G. Kostryzhev, A.A. Saleh, L. Chen, and E.V. Pereloma: *Mater. Sci. Eng. A*, 2016, vol. 664, pp. 26–42.
37. Z.P. Xiong, A.G. Kostryzhev, L. Chen, and E.V. Pereloma: *Mater. Sci. Eng. A*, 2016, vol. 677, pp. 356–66.
38. Z.P. Xiong, A.G. Kostryzhev, N.E. Stanford, and E.V. Pereloma: *Mater. Des.*, 2015, vol. 88, pp. 537–49.
39. Z.P. Xiong, A.G. Kostryzhev, N.E. Stanford, and E.V. Pereloma: *Mater. Sci. Eng. A*, 2016, vol. 651, pp. 291–05.
40. Z.P. Xiong, A.A. Saleh, R.K.W. Marceau, A.S. Taylor, E.V. Pereloma, N.E. Stanford, A.G. Kostryzhev, and E.V. Pereloma: *Acta Mater.*, 2017, vol. 134, pp. 1–15.
41. P.S. Lyu, W.L. Wang, and H.H. Zhang: *Metall. Mater. Trans. B*, 2017, vol. 48B, pp. 247–59.
42. P.S. Lyu, W.L. Wang, X.K. Long, K.X. Zhang, E.Z. Gao, and R.S. Qin: *Metall. Mater. Trans. B*, 2018, vol. 49B, pp. 78–88.
43. J.V. Beck and K.A. Woodbury: *Meas. Sci. Technol.*, 1998, vol. 9, pp. 839–47.
44. J.V. Beck, B. Litkouhi, and C.S. St. Clair: *Heat Transfer A*, 1982, vol. 5, pp. 275–86.
45. H.H. Zhang, W.L. Wang, D. Zhou, F.J. Ma, B.X. Lu, and L.J. Zhou: *Metall. Mater. Trans. B*, 2014, vol. 45B, pp. 1038–47.
46. D. Zhou, W.L. Wang, H.H. Zhang, F.J. Ma, K. Chen, and L.J. Zhou: *Metall. Mater. Trans. B*, 2014, vol. 45B, pp. 1048–56.
47. M. Ferry: *Direct Strip Casting of Metals and Alloys*, Woodhead Publishing, Cambridge, 2006.
48. O. Kubaschewski: *Iron Binary Phase Diagram*, Springer, Berlin, 1982.
49. T. Dorin, A. Taylor, K. Wood, J. Wang, P. Hodgson, and N. Stanford: *J. Appl. Crystallogr.*, 2016, vol. 49, pp. 1777–85.
50. T. Dorin, N. Stanford, A. Taylor, and P. Hodgson: *Metall. Mater. Trans. A*, 2015, vol. 46A, pp. 5561–71.
51. K. Oikawa, H. Ohtani, K. Ishida, and T. Nishizawa: *ISIJ Int.*, 1995, vol. 35, pp. 402–08.
52. S. Wang, Y.F. Liang, B. Chen, F. Ye, and J.P. Lin: *Metals*, 2018, vol. 8, p. 259.
53. Y.F. Liang, F. Ye, J.P. Lin, Y.L. Wang, and G.L. Chen: *J. Alloys Compd.*, 2010, vol. 491, pp. 268–70.
54. A.H. Kasama, C. Bolfarini, C.S. Kiminami, and W.J.B. Filho: Magnetic properties evaluation of spray formed and rolled Fe–6.5 wt pct Si–1.0 wt pct Al alloy: *Mater. Sci. Eng. A*, 2007, vol. 449, pp. 375–77.
55. H. Haiji, K. Okada, T. Hiratani, M. Abe, and M. Ninomiya: *J. Magn. Magn. Mater.*, 1996, vol. 160, pp. 109–14.

Publisher's Note Springer Nature remains neutral with regard to jurisdictional claims in published maps and institutional affiliations.